Identification of degradation mechanisms in slot-die coated non-fullerene ITO-free organic solar cells using different illumination spectra

Belén Arredondo[†], Gonzalo del Pozo[†], Enrique Hernández-Balaguera[†], Diego Martín Martín[†], María del Carmen López González[†], Beatriz Romero[†], Eduardo López-Fraguas[‡], Ricardo Vergaz[‡], Xabier Quintana[††], Jani Lamminaho[ɻ], Elodie Destouesse[ɻ], Mehrad Ahmadpour[ɻ],Vida Turkovic[ɻ], Morten Madsen[ɻ].*

[†]Área de Tecnología Electrónica, DELFO, Universidad Rey Juan Carlos, C/ Tulipán s/n, 28933, Móstoles, Spain.

[‡]Departamento de Tecnología Electrónica, GDAF-UC3M, Universidad Carlos III de Madrid, Leganés 28911, Spain

[††]Departamento de Tecnología Fotónica y Bioingeniería, CEMDATIC, Universidad Politécnica de Madrid, 28040 Madrid, Spain.

[ɻ]SDU NanoSYD, Mads Clausen Institute, University of Southern Denmark, Alsion 2, 6400 Sønderborg, Denmark.

KEYWORDS: Organic solar cells, degradation, non-fullerene, slot-die coating, ITO-free, flexible.

ABSTRACT: In this work we have studied degradation mechanisms of non-fullerene based organic solar cells with PET / Ag / ZnO / PBDTB-T:ITIC / PEDOT:PSS / CPP PEDOT:PSS device structure. We compare pristine and degraded samples that were subjected to outdoor degradation following standard ISOS-O2 protocol. The ideality factors for different incident wavelengths obtained from open circuit voltage versus irradiation level and current density-voltage (*J-V*) measurements at different temperatures, indicate that for aged samples recombination is governed by Shockley-Red-Hall mechanism occurring in a region near the anode. Samples were also characterized using impedance spectroscopy and fitted to an electrical model. Impedance parameters were used to obtain mobility, indicating a clear degradation of the active layer blend for aged samples. The change in the chemical capacitance also reveals a worsening in carrier extraction. Finally, 2D numerical simulations and fits to experimental *J-V* curves confirm the existence of a layer near the anode contact with poorer mobility and a decrease of the anode work function for the degraded samples.

INTRODUCTION

Most common organic solar cells (OSCs) are based on a solution-processed bulk heterojunction (BHJ) layer composed of a conjugated polymer as donor and typically a fullerene derivative as electron acceptor ($PC_{60}BM$/$PC_{70}BM$). To date, BHJ solar cells using fullerene acceptors typically exhibit a power conversion efficiency (PCE) of around 5% [1], and rarely exceeding 10% [2–4], mainly due to several fullerene related drawbacks such as difficulty in tunability of the electronic

molecular levels that limits the open circuit voltage, and limited light absorption. Likewise, extensive work has been carried out in understanding the degradation mechanisms of fullerene based OSCs [5–13].

In the past years great efforts have been dedicated to synthesize new acceptors with easily tuneable properties by chemical modification. In this context, non-fullerene acceptors have become widely popular because of their outstanding optical absorption, good electron transport mobility, easily adjustable optical bandgap, low synthetic cost, and good miscibility with polymers [14–20]. Several works reported fullerene-free devices with boosted PCE of around 14-16% in single junction solar cells [18,21–24]. The ease with which energy levels are tuned opens the possibility to optimize light harvesting in different spectral regions, synthesizing acceptors with absorption regions complementary to those of the donor material, and facilitates devices with open circuit voltages above 1.1 V and low voltage losses [25,26].

Nevertheless, to our knowledge, not many studies have been carried out on the degradation and stability of fullerene-free solar cells. Few works reveal that non-fullerene devices show good stability in air and under dark storage [27,28]. However, Doumon et al. performed a comparative study on photo-stability of PBDB-T:ITIC versus a standard fullerene solar cell based on PBDB-T: $PC_{70}BM$ [29]. These fullerene-free solar cells were first reported by Zhao et al. with PCE over 11% using a combination of the conjugated polymer PBDTB-T (poly[(2,6-(4,8-bis(5-(2-ethylhexyl)thiophen-2-yl)-benzo[1,2-b:4,5-b']dithiophene))-alt-(5,5-(1',3'-di-2-thienyl-5',7'-bis(2-ethylhexyl) benzo[1',2'-c:4',5'-c']dithiophene-4,8-dione))]) as donor and a small molecule ITIC (3,9-bis(2-methylene-(3-(1,1-dicyanomethylene)-indanone))-5,5,11,11-tetrakis(4-hexylphenyl)-dithieno[2,3-d:2′,3′-d′]-s-indaceno[1,2b:5,6-b′] dithiophene) as acceptor [14]. Doumon et al. concluded that although ITIC based solar cells performed better in terms of initial PCE, they

exhibited poorer photo-stability than $PC_{70}BM$ based devices due to lowered mobility upon light exposure for the investigated system. Similar was observed by Upama et al., who assigned the PBDB-T:ITIC devices degradation to broadening of Urbach energy and subsequent increase in the energetic disorder in the active layer, as well as the increased exponential distribution of localized states which act as trap-mediated recombination centers [15]. Du et al. assigned this increase of energetic traps in ITIC, ITIC-M and ITIC-DM based systems to the breaking of conjugation, and found that fluorination as well as avoidance of methyl groups of the end-group stabilizes the molecules against photooxidation [30]. They also observed a reorientation of ITIC molecules in the blend from face-on to edge-on upon degradation, which further negatively affects the efficiency. Further importance of the molecular structure and conformation on the photostability of NFA-based systems in air was demonstrated by Luke et al., who observed less initial photoinduced conformational change induced by noncovalent interactions with environmental molecules in case of the planar IDTBR leading to a stronger photostability as opposed to amorphous nonplanar IDFBR [31]. Recently, a relation between the stability and the LUMO levels of the non-fullerene acceptors was reported, where the yield of the highly reactive radical superoxide anions is strongly enhanced in lower lying LUMO NFAs, which negatively affects their photostability, as the superoxide radical anion initiates the radical chain oxidation of the active layer [19]. Thus, these few initial studies on the stability of fullerene-free solar cells underline the NFA-specific, yet non-revealed degradation mechanisms, which need to be further investigated and better understood in order to provide long lifetimes to these otherwise highly efficient devices.

In this work, we have studied the dominant recombination mechanisms and active layer transport properties occurring in a solar cell based on the polymer PBDTB-T, blended with the acceptor molecule ITIC on a polyethylene terephthalate substrate with structure PET / Ag / ZnO / PBDTB-

T:ITIC / HTL PEDOT:PSS / CPP105D PEDOT:PSS. Current density-voltage (*J-V*) and Impedance Spectroscopy (IS) measurements with equivalent-circuit analysis and physical modelling are used to investigate the dynamical processes governing the device. Moreover, impedance spectra using two monochromatic illuminations (λ = 630 nm and λ = 450 nm), and *J-V* curves for varying temperatures provide information about mobility and activation energy of the dominant carrier recombination path. Finally, we have performed numerical device simulation using SILVACO ATLAS to support the conclusions obtained from the experiment.

EXPERIMENTAL METHODS

The OPV structure used in this study is presented on Figure 1c. A heat stabilized PET foil with a thickness of 125 µm (Melinex ST504) from DuPont Teijin Films was used as substrate. ZnO Nanoparticles (H-SZ01034) were purchased from Genes'ink and were in-line filtered with a 0.2 µm RC filter from Whatman. PBDB-T and ITIC were purchased from Brilliant Matters Inc. The active layer solution was prepared with a ratio 1:1 (PBDB-T: ITIC) at a total concentration of 30 mg/ml in chlorobenzene with 0.5% v/v of 1.8-diiodooctane. The solution was stirred at 80°C for 3 hours in ambient conditions. PEDOT:PSS (HTL solar and CPP105D) were both purchased from Heraeus. 10% v/v of silver nanowires in isopropanol were added to the CPP105D prior to deposition, in order to increase the conductivity of the top electrode.

Organic solar cells were fabricated in the following inverted device configuration: PET/Ag/ZnO/PBDB-T: ITIC/HTL PEDOT:PSS/CP105D PEDOT:PSS. All devices were processed in ambient conditions, except for the vacuum deposited bottom electrode. For silver deposition, the PET substrates were pretreated with DC argon plasma in vacuum.

Silver electrodes (around 100nm) were deposited using DC magnetron sputter (power 150 W, pressure 6·10-3 mbar, time 170 s), through a shadow mask that defines the small-scale cell or module area. The whole process was done in a R2R vacuum line. Solution based slot-die coatings were performed using a motorized film applicator (Erichsen COATMASTER 510), which was custom modified for slot-die coating. The coating system holds a vacuum plate containing a heating element, for combined substrate fixture and substrate heating. A syringe pump (Harvard Apparatus PHD 2000) was used for controlled ink delivery. During coating, the syringe can be heated in a custom-build aluminum sleeve with silicone heater pads. The slot-die head was custom-built from stainless steel, and the heating of the slot-die head was done with a heating cartridge. Shims and meniscus guides were used to limit coating widths to 11 mm with ETL and active layer. In case of PEDOT:PSS HTL and CPP105D, shim and meniscus guide were used to limit coating width to 7 mm. The vacuum plate was heated to 70°C before the coating process was started, and kept at this temperature throughout the coating process. The slot-die coating steps were performed under ambient air. Used coating parameters with resulting film thicknesses can be seen in Table 1.

Table 1. Slot die coating parameters and layer thicknesses.

	Fabrication details				
	Pumping speed (ml/min)	Coating speed (mm/s)	Coating gap (μm)	Thickness (nm)	Annealing
ZnO	0,05	12	200	30	100 °C (10 min)
PBDB-: ITIC	0,035	6,3	200	300	-
PEDOT: PSS HTL	0,06	7	200	100	-
PEDOT:PSS CPP105D	0,05	7	250	100	65 °C (5 min) 60 °C (5 min)

During the active layer coating process, both the slot-die head and the syringe were heated to 60°C. The PEDOT:PSS HTL Solar solution was coated directly following coating of the active layer. Annealing of the foils after ZnO and at the very end (the complete layer stack) was performed in vacuum oven. PET foil dimensions were 350 mm x 100 mm containing 60 samples in four rows. Each sample contained four devices that had an active area of 5.4 mm^2. The cell layout on the PET foil is seen in figure 1a, and more details on the development of the cells from scalable fabrication methods can be found in [32].

Finally, samples were cut from the foil and glued (Permabond 105) on glass substrate followed by encapsulation with a round glass cover. Delo KATIOBOND LP655 was used as encapsulation glue, which was cured under UV light. Encapsulated samples and layer structure can be seen in figures 1b and 1c respectively.

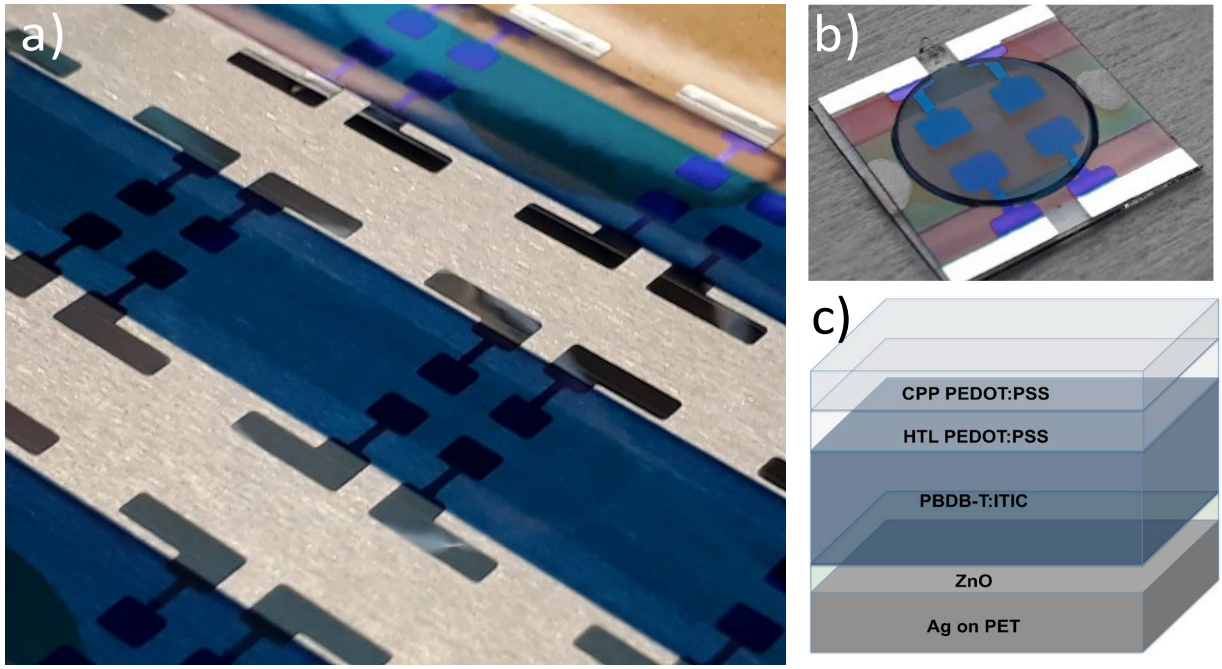

Figure 1. a) Cell layout on PET foil, b) Encapsulated sample c) Layer structure

Spectral response characteristics (external quantum efficiency, EQE) were taken using a custom-made system based on a Xe lamp light source and a double grating monochromator. The system is equipped with a monitor cell to compensate for temporal fluctuations in the light source. Chopped light together with a lock-in amplifier are used to maximize the signal-to-noise ratio.

Electrical measurements were carried out using an AutoLab Potentiostat/Galvanostat model PGSTAT204 (Eco-Chemie), equipped with the FRA32M impedance module and the Metrohm AutoLab optical bench. The instrument was controlled by a computer and driven by NOVA 2.1.4 software. Experimental *J-V* characteristics were obtained performing a cyclic voltammetry test from –0.3 V to 1.2 V. Impedance Spectroscopy (IS) measurements were carried out immediately after *J-V* experiments, by configuring the AutoLab to apply sinusoidal signals of 50 mV amplitude from 1 MHz to 1 Hz under open-circuit conditions. Fitting of all the impedance spectra were performed using Scribner's ZView software. Both techniques were performed for three illumination spectra (under white, blue, and red illuminations), varying illumination intensities from 1 up to 10 or 100 mW/cm^2 for blue and red, or white, respectively, using a calibrated silicon photodiode. Under white illumination conditions, the photovoltaic cell performance was analyzed using a Newport VeraSol-2 LED class AAA solar simulator calibrated with an NIST-certified KG3 filtered Si reference cell.

Outdoor lifetime testing was carried out according to International Summit on OPV Stability (ISOS) standard O-2 protocol [33]. The degradation of the samples was carried out in two periods of the year with different environmental conditions. Therefore a "dry" and a "wet" degradation can be distinguished. The wet degradation has been performed over a period of 525 hours (22 days) with 131.3 equivalent hours of sun, 59.13% average humidity (with 28.5% and 94.8% as the lowest and highest values), and -1.6 ºC/17.3 ºC minimum/maximum temperature. It is worth

noticing that the maximum humidity corresponds to rainy days, thus causing the samples to get wet. The dry degradation has been carried out along 216 hours (9 days) with 86.6 equivalent hours of sun, 38.4% average humidity (between 15.5% and 71.3%), and 10.2 ºC/30.6 ºC minimum/maximum temperature.

Furthermore, the open-circuit potential was measured at different temperatures (from 293 K to 333 K) in order to analyze the temperature-dependent device characteristics. The measurements were performed inserting the cells in an TS102GXY hot/cold stage by Instec, operated under 24 V (DC) and 5 A. A 100 W platinum RTD is its temperature sensor. The stage contains a PID-controlled mk2000 Peltier that allows an accurate temperature setting (±0.05 ºC) in the range explored in this work. We used a water-cooling pump system to guarantee stage temperatures below room temperature. In this experiment, we irradiated our cell using a proprietary LED-based sun simulator called SUNBOX. It is a class AAA device that allows the characterization of devices of 2x2 cm, placed on a platform 5 cm under a 34 LEDs PCB, in which every spectral set of LEDs can be controlled separately [34].

Finally, the characterization was performed on four samples, with 4 devices each, that is, a total of 16 nominally equal devices. All devices were characterized in the pristine state showing similar DC/AC electrical behavior. Statistical information (average values and standard deviation) of PCE, FF, J_{SC} and V_{OC} can be found in the Supplementary Information.

RESULTS AND DISCUSSION

Inset in Figure 2a shows the energy levels schematic. The energy difference between the HOMO of PBDB-T and the LUMO of the ITIC provides an effective bandgap energy for the blend of 1.55

eV. Besides, the reduced energy barrier between the HOMO levels of the donor and the acceptor reduces the energy losses in the generation of free carriers.

Previous works show the complementary absorption spectra of the acceptor ITIC and the donor PBDTB-T [14,35], enhancing the initial device performance with respect to fullerene based cells. This is confirmed with our EQE measurement shown in Figure 2a, with the appearance of spectral response characteristic extended to 800 nm, compared to cells based on PBDTBT:PCBM with no quantum efficiency in that part of the spectrum [36].

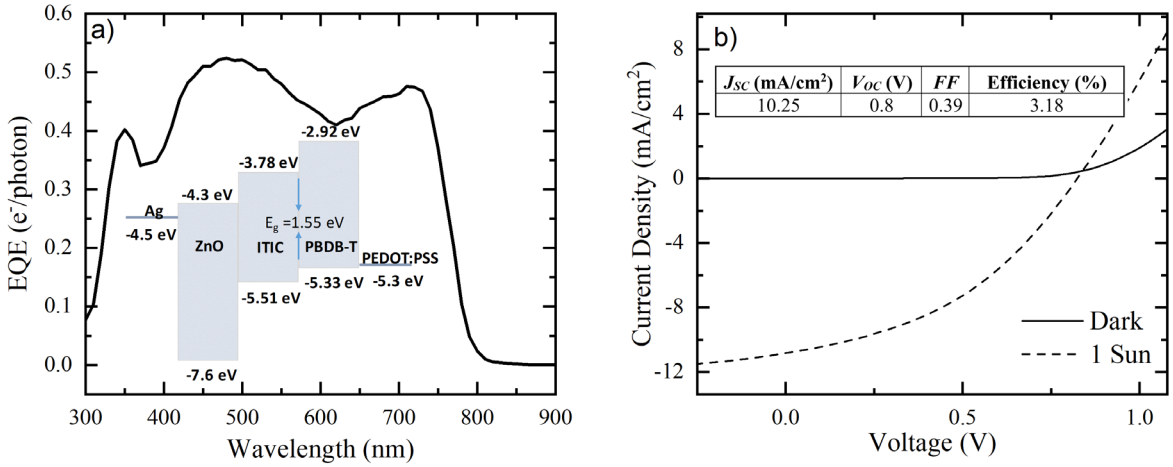

Figure 2. a) External quantum efficiency (EQE). Inset shows the energy levels diagram. b) *J-V* characteristic in dark and under 1-sun illumination AM1.5 (100 mW/cm^2) of the pristine device.

In a previous study the cell performance evolves positively during an ISOS-D-1 study in which the cells were illuminated when measured [32]. We note that also illumination of active layer cells in nitrogen has shown to provide a minor positive evolution in performance during the initial illumination phase in a different study. Moreover, we note that the conductivity of ZnO can also be improved with exposure to UV-light, and thus, power conversion efficiency also increases [37]. Thus, devices were pre-treated with irradiation from a solar simulator for a short time (approx.60 sec) in order to ensure maximum performance (long illumination times could result in degradation

of the active layer system). *J-V* characteristics in dark and under 1 sun illumination, and the corresponding performance parameters are shown in Figure 2b. Fresh devices exhibit moderate efficiency compared to previous related studies with cells based on the same active layer blend but different layer structure [14,29]. Also, devices show modest efficiency when compared to previous studies with ITO-free non-fullerene flexible OSCs with different active layer [38]. At this point, we emphasize that cells presented in this work are developed under industrial conditions from scalable processes in air (S2S slot-die coating), using flexible substrates and ITO-free electrodes. Combined, the expected efficiency is thus also lower than the typically reported for this active layer material system or for other ITO-free non-fullerene systems. In order to further explain the initial low performance of the cells, we show the AFM images of PCE12:ITIC films developed from spin-coating and slot-die coating (see Fig. S1 of the Sup. Info.). A further optimization of this cell configuration is demonstrated in [32]. At this point, it is not the aim of this work to maximize the efficiency, but to investigate the stability and degradation pathways of cells fabricated without using fullerene and ITO. It is worth pointing out that the below experiments using different excitations wavelengths were carried out for degraded samples when the efficiency had gone down to 0.4%. The full lifetime plot is shown in the Supplementary Information.

According to Figure 3, the ideality factors (*n*) of the fresh and degraded samples under dry conditions are obtained from the slope of the logarithmic fit of the open-circuit voltage (V_{OC}) vs. illumination intensity (irradiance) with different light spectra; red, blue, and white light illumination. Using different excitation wavelengths, we can obtain information about the penetration depth of the optical input inside the active layer. The absorption in the red part of the spectrum is much more intense than in the blue region [14,32], and since EQE is around 0.5 for the blue and 0.42 for the red light (that is only a 15% difference, see Figure 2a), it follows from the

Beer-Lambert law, that red light is absorbed near the anode contact, while blue light penetrates deeper in the layer. In order to support this thesis, we have performed simulations using Silvaco TCAD of transmissivity and absorptivity as function of the active layer depth for blue (450 nm) and red (630 nm) monochromatic illuminations (see Fig.S2 of the Supplementary Information). Our simulations validate our statement about the more intense absorption of red light near the anode contact. Thus, the value of the ideality factor, corresponding to the red and blue light illumination, is related to recombination mechanisms taking place in different spatial regions of the device. Moreover, the fact that open-circuit voltage tends to saturate with light intensity indicates the presence of non-selective contacts [39]. Note that this effect is more pronounced in the case of the degraded sample as shown in Figure 3. Ideality factors obtained from the fits are summarized in Table 2. The values found indicate a Shockley-Read-Hall (SRH) recombination mechanism for red- and blue-light illumination in pristine samples (n values of 1.2 and 1.5, respectively). In contrast, n is around 1 for the aged devices under red light illumination, while it remains unchanged for blue light excitation. This indicates that the degradation is mostly affecting the space near the anode, where the red wavelength is being strongly absorbed. This result is in good agreement with Wang et al., who demonstrated that interfacial reaction between PEDOT:PSS hole transport layer and ITIC acceptor was one of the main responsible mechanisms for non-fullerene OSC deterioration[40]. In a MIM (metal-intrinsic-metal) device or p-i-n cell with low mobility and an homogenous electric field across the device, an ideality factor of $n \approx 1$ indicates that the recombination near the contact dominates [39]. Numerical simulations are shown in the last section of the article corroborating that these devices indeed behave as p-i-n cells. Hence, we can infer that, for the aged devices, recombination presumably takes place in an Interfacial Damaged Layer (IDL) near the anode due to an increase of traps. The activation energy of these

recombination centres will be analysed later using temperature measurements. Furthermore, diode ideality factor, before (fresh) and after degradation exposed to white-light, follows those trends obtained with red wavelength excitation, indicating that recombination near the anode is the dominant mechanism even when illuminating with the whole spectrum. This hypothesis is reinforced by the fact that, for the degraded diodes, V_{OC} under red and white illuminations overlap, while for the blue light, open-circuit voltage is slightly above. Note that the illumination intensity range covered by the red and blue colours cannot go beyond 10 mW/cm^2 corresponding to the maximum achieved by our LED set-up.

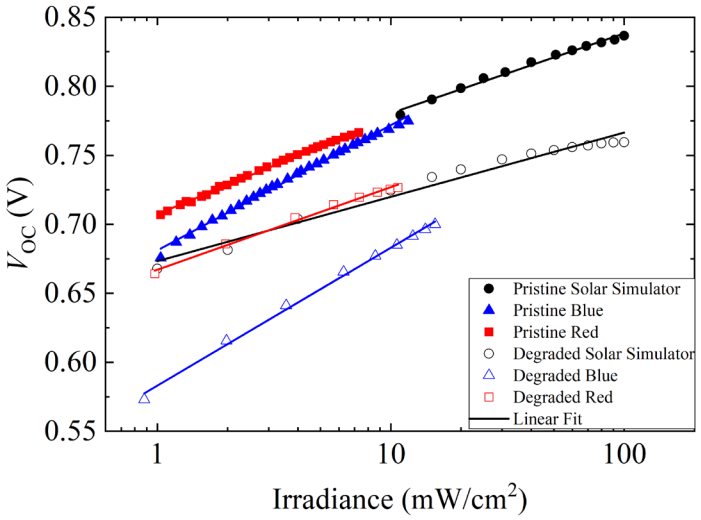

Figure 3. Open-circuit voltage (V_{OC}) vs. light intensity for fresh and dry-degraded samples for white, red, and blue illumination. Ideality factor (n) is obtained from the slope, $-q/(nk_BT)$, of the linear regression.

Table 2. Ideality factors obtained from the fits shown in Figure 3 for the fresh and the degraded devices, using three illumination spectra; $\lambda = 630$ nm (red), $\lambda = 450$ nm (blue), and white light.

	n		
	Red	Blue	White
Pristine	1.2	1.5	1
Degraded	1	1.5	0.8

Figure 4 shows the fill factor (*FF*) vs. irradiance for pristine and degraded samples and for λ = 630 nm, λ = 450 nm, and white illumination (the latter shown in the inset). The origin of the *FF*, obtained from the *J-V* curves, is determined by carrier extraction and carrier recombination, both competing processes governed by the mobility. As indicated in recent reports, there is an optimized mobility at which efficiency and *FF* is maximum; for higher light intensities, carrier recombination increases, deteriorating the *FF* and power conversion efficiency [41]. In our study, *FF* values corresponding to blue illumination for the fresh cells, remain almost unchanged with increasing irradiance. In contrast, when exposed to red light, the *FF* decreases slightly with light concentration. Degraded samples exhibit, as expected, a reduced *FF* that decays abruptly with light. Moreover, for white illumination, a similar behaviour was identified to that obtained using the red wavelength excitation (refer to the inset of Figure 4). Later in the paper we will discuss the influence on the *FF* of the mobility obtained from IS measurements.

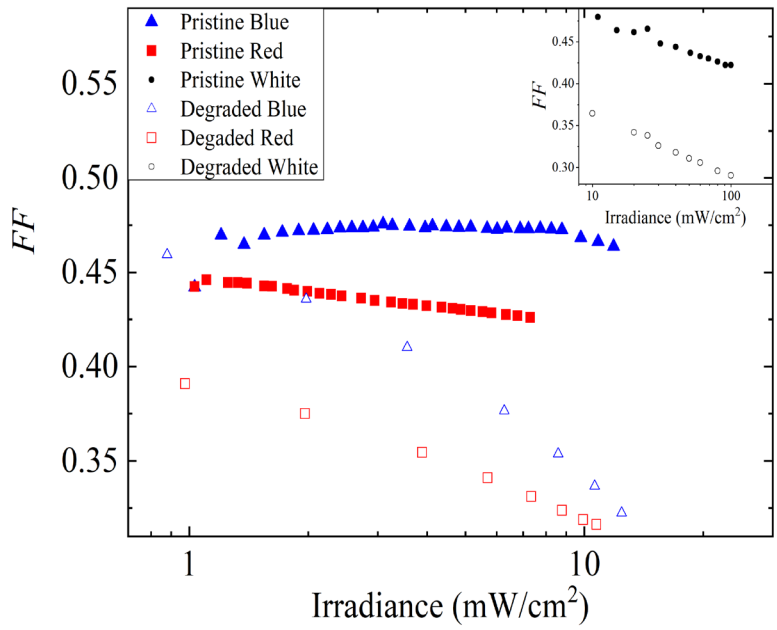

Figure 4. Fill factor (*FF*) vs. irradiance for pristine and degraded samples illuminated with wavelengths of λ= 630 nm (red) and λ =4 50 nm (blue). Inset shows *FF* values, for fresh and aged devices, at different illumination levels of white light.

Figure 5 shows representative examples of the experimental impedance spectra for the fresh a) and degraded b) samples at different color intensities measured at V_{OC}. Solid lines correspond to the fits using the equivalent electrical circuit of the inset (Matryoshka circuit). This circuital model has been widely used in previous works [5,6] and consists of a series resistance R_S (associated with ohmic losses at soldering and external wires), a recombination resistance R_P, a transport resistance R_T, a geometrical capacitance C_g, and a constant phase element (CPE) with impedance, $Z_{CPE}(j\omega)=\frac{1}{Q(j\omega)^{\alpha}}$, connected as shown in the inset of Figure 5. Note that Q (with units of $F\times s^{\alpha-1}$) and α (over the range 0 to 1) are the CPE's parameters, j is the imaginary unit, and ω is the angular frequency ($\omega=2\pi f$ where f is frequency). Figure 5 exhibits an excellent agreement between the experimental and simulated data. The shape of the Cole-Cole curves is similar for the three

illumination spectra used, for pristine and degraded samples, displaying: (i) a capacitive loop at sufficiently high frequencies, related to carrier diffusion transport phenomena with a large active layer thickness (L=220 nm); and (ii) a depressed semicircle at the low-frequency region, attributed to the recombination process, which involves a frequency dispersion the of experimental impedance data. This CPE behaviour that models a non-ideal chemical capacitance leads to a time-constant distribution whose average characteristic value is, $\tau_{lf}=(R_P Q)^{1/\alpha}$. Using this expression, an effective capacitance associated with the CPE can be found by matching the distributed time-constant and that of the ideal RC time-constant ($\tau_{lf}=R_P C_\mu$), yielding $C_\mu=R_P^{1-\alpha/\alpha} Q^{1/\alpha}$ [42]. Importantly, a characteristic feature associated to the diffusion time can be obtained from the effective chemical capacitance: $\tau_d=R_T C_\mu$. Note that throughout this paper, τ_d provides valuable information on the device degradation associated to charge carrier mobilities.

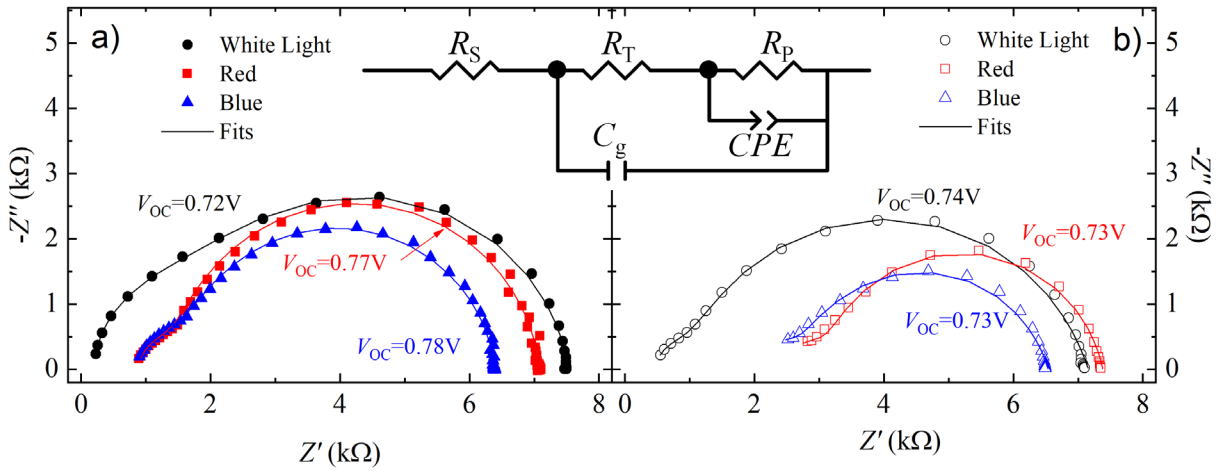

Figure 5. Experimental impedance spectra, under open-circuit conditions, for white, red, and blue illumination for a) fresh and b) degraded samples. Solid lines indicate the simulated results using the electrical equivalent circuit shown in the inset.

Figure 6 shows the dependence of the impedance parameters with V_{OC} obtained from the fit of the circuital model to IS measurements under red and blue illuminations. Impedance parameters under white illumination for pristine and degraded devices cannot be compared since V_{OC} ranges do not overlap, as shown in Figure 3. Impedance parameters for red and blue illumination in pristine and degraded samples are discussed below: (i) C_g remains almost constant ($C_g \approx 0.87$ nF) with open-circuit voltage for pristine devices, since its value is related to the geometrical capacitance of the active layer (refer to Figure 6c). Thus, the dielectric constant of the absorbing organic layer can be found from $C_g = \varepsilon\varepsilon_0 A/L$, resulting in $\varepsilon \approx 3.68$; where ε_0 is the permittivity of vacuum, A is the device area and L is the active layer thickness. It is noteworthy that the value of C_g slightly increases after degradation, particularly at high irradiation levels, which is typically attributed to device heating. Indeed, high illumination intensities must be applied after the degradation experiment to reach comparable open-circuit voltages. (ii) Both resistances, R_T and R_P, decrease with the radiation intensity, as expected (see Figures 6a and 6b, respectively). R_T increases with degradation for both colours indicating that conduction is limited by the transport mechanisms. On the other hand, R_P decreases during the degradation process, indicating an increase of recombination, in particular for red illumination, which is in good agreement with the trend of the ideality factor for this colour. (iii) Finally, it is important to point out that degradation significantly modifies the value of the effective chemical capacitance shown in Figure 6d (extracted from the CPE parameters, see above). This variation suggests an inefficient charge extraction. From a mathematical point of view, we can explain this using the dependence of C_μ value on Q and α parameters. Indeed, the value of C_μ depends critically on $Q^{1/\alpha}$, which increases upon degradation reflecting a worsening of carrier extraction and a higher degree of disorder in the material (α value approximately decays from 0.9 down to 0.7, driving away C_μ from a purely

capacitive behaviour). This worsening in carrier extraction can be also related to a reduction of the anode work function, as will be discussed in the last section of the article.

For comparative purposes, the exponential dependence of R_P with V_{OC} shown in Figure 6b, with characteristic slope $-q/(nk_BT)$, where T is the temperature and k_B is the Boltzmann constant, allows the calculation of the ideality factor. For fresh samples n equals 1.6 (red) and 1.7 (blue), while for the aged devices n is 1.2 (red) and 1.6 (blue). In effect, a close inspection of the n values reveals a high degree of similarity between the tendencies obtained for DC measurements (refer to Table 2) and those found using the IS technique.

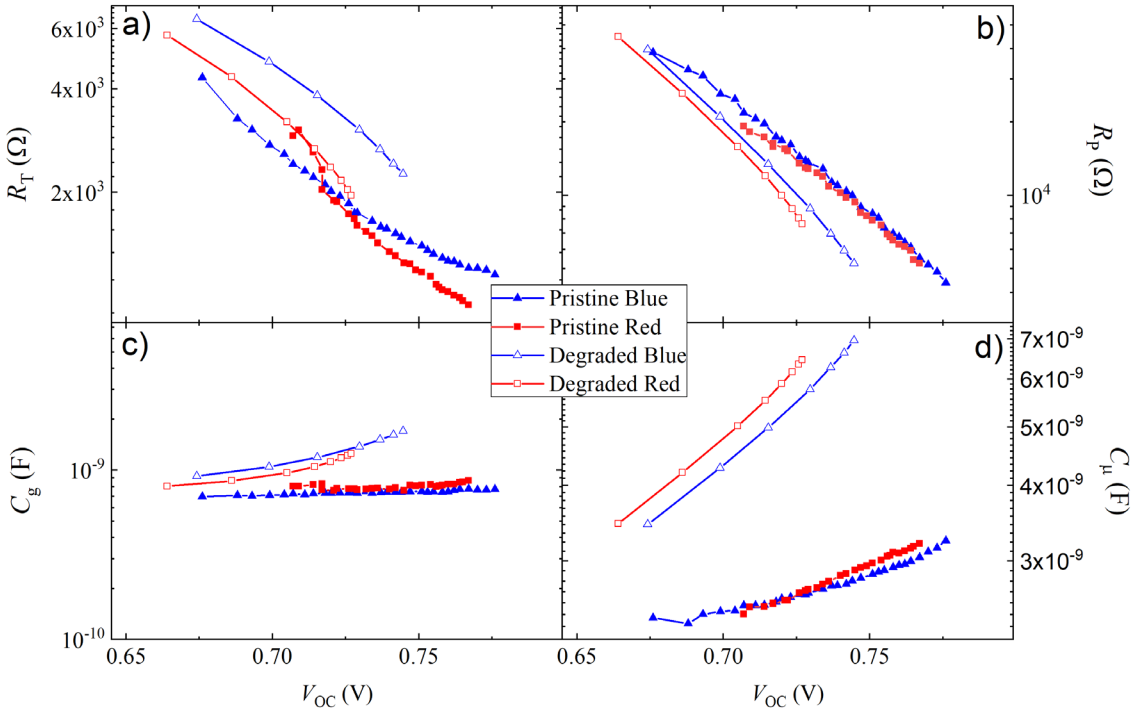

Figure 6. Evolution of parameters obtained from the impedance results using Matryoshka circuit at open-circuit conditions for fresh and aged devices. a) Transport resistance, R_T; b) recombination resistance, R_P; c) geometrical capacitance, C_g; and d) effective chemical capacitance, C_μ (associated to low-frequency R-CPE sub-circuit).

The electron mobility at open-circuit voltage can be estimated using $\mu = {L^2}/{\tau_d V_T}$ where V_T is the thermal voltage ($V_T = k_B T/q$). Table 3 shows the value of the mobilities obtained before and after degradation for all the excitation wavelengths. Mobility for red and blue excitation exhibits a higher decrease than that obtained with white light illumination. Furthermore, mobilities in the pristine devices exhibit similar values for red and blue illumination, and thus, the smaller *FF* for the red light shown in Figure 4 cannot be attributed to a change in mobility. This reduced *FF* and its decreasing trend with the irradiance for red light in the fresh sample can only be related to higher recombination for red wavelengths near the anode as indicated by the ideality factor. In the case of the degraded samples, the mobility decreases by a factor of three, and therefore it governs the abrupt decrease of *FF* versus light intensity for all colours. This is a consequence of the increase of R_T for the degraded samples, suggesting that the conduction is greatly limited by carrier transport after the ageing process.

Table 3. Average carrier mobility values obtained for fresh and aged samples under 10 mW/cm^2 for blue and red light, and 100 mW/cm^2 for white light.

	Mobilities ($cm^2 \times V^{-1} \times s^{-1}$)		
	Red	Blue	White
Pristine	6.2×10^{-3}	5.1×10^{-3}	1.9×10^{-2}
Degraded	2.0×10^{-3}	1.6×10^{-3}	7.9×10^{-3}

In order to gain further insight in the active layer degradation with time as the sample suffers the outdoor degradation protocol, the Density of States (DOS) has been obtained from the chemical capacitance. Specifically, DOS has been calculated fitting the chemical capacitance with Eq. 1,

where N_n is the total density of states, and E_L and σ_n the centre and width of the DOS, respectively [43].

$$g_n(E - E_L) = \frac{N_n}{\sqrt{2\pi\sigma_n}} \exp\left[-\frac{(E_L - E)^2}{2\sigma_n^2}\right] \qquad (1)$$

The fits of Eq. 1 to the experimental chemical capacitance shown in Figure 7a as solid lines indicate a broadening of the DOS width with time under outdoor exposure. It is worth mentioning that the increase of the DOS width shown in Figure 7b corresponds to the days of measurement just after the first rainy days of the outdoor experiment. Though this DOS width values may present great uncertainty, the trend indicates an increasing degree of disorder in the active layer blend. This trend in σ_n is not observed when analysing samples undergoing indoor degradation, or samples undergoing outdoor degradation that were not exposed to rain (dry degradation, see Sup. Info). This suggests that moisture is the main cause of the deterioration of the PBDTB-T:ITIC blend morphology.

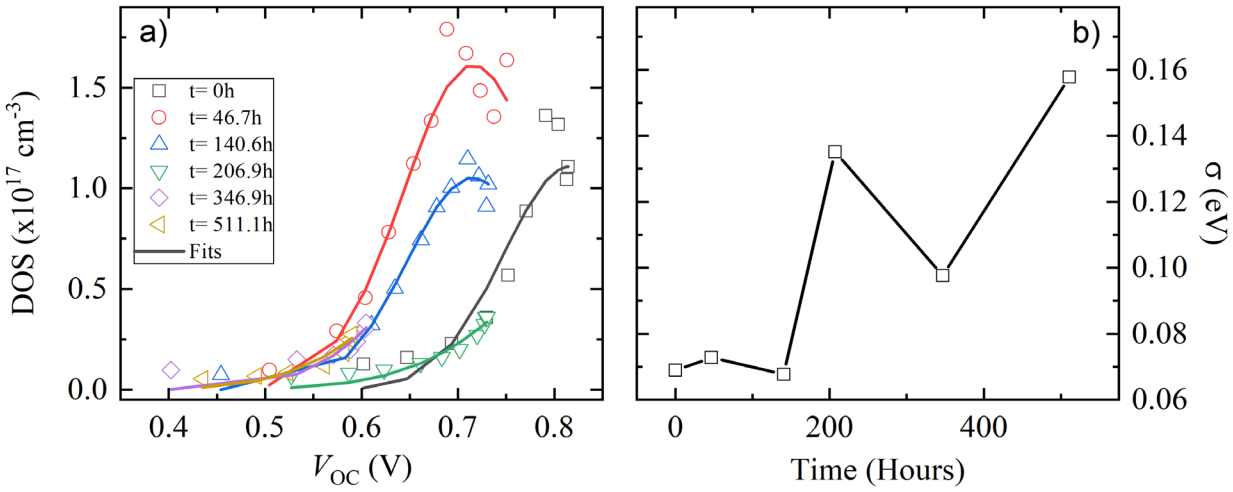

Figure 7. a) Evolution of the Gaussian DOS parameters at the LUMO of ITIC obtained by fitting the chemical capacitance extracted from impedance at V_{OC} under different irradiances using Eq.

(1). b) Width of the DOS (σ) as a function of the degradation time, for the sample exposed to the outdoor degradation under high humidity levels.

Temperature-dependent *J-V* measurements under white light at varying illumination levels in the pristine conditions are shown in Figure 8a. Linear decays (V_{OC} vs. T), at all light-intensity experiments (from 20 up to 120 mW/cm^2, equivalent to 1.2 suns), can be observed. Open-circuit voltage as a function of temperature for all illumination levels was fitted to a linear regression. When the straight lines V_{OC}-T are extrapolated towards the axis at $T = 0$ K, V_{OC} correlates with the activation energy E_a of the recombination process [44]. The values obtained for E_a have been represented as a function of the illumination level as shown in Figure 8b, where the activation energy decreases as the light intensity is increased. Comparing the obtained values of E_a with the donor-acceptor bandgap E_g (≈1.55 eV, see inset Figure 2a), smaller values of the activation energy are revealed ($E_a < E_g$), suggesting that the recombination mechanism is dominated by the mid-gap recombination centres [44]. Thus, this reinforces the thesis of SRH recombination phenomena in an IDL near the interface region as indicated by the n values obtained previously. Moreover, the decreasing trend of E_a with light intensity shown in Figure 8b is related to the energy distribution of the trap filling mechanism within the gap.

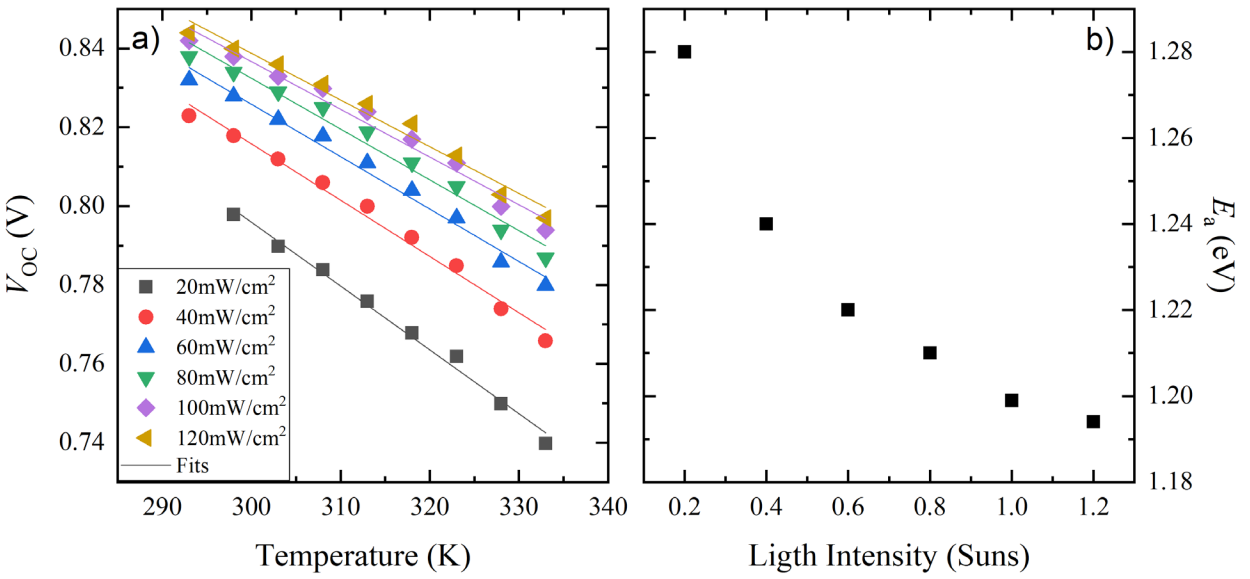

Figure 8. a) Open-circuit voltage V_{OC} (extracted from current density-voltage curves) as a function of temperature under varying illumination conditions. b) Activation energy E_a of the recombination process (obtained from the linear fit of V_{OC}-T characteristic) vs. light intensity.

Finally, devices have been modelled using Silvaco ATLAS (see Sup. Information for further details). 2D numerical simulations have been performed to consolidate our understanding of the dynamical mechanisms taking place inside the cells during degradation. Figure 9a shows both experimental and simulated *J*-*V* characteristics under 1-sun illumination AM1.5G for the pristine and degraded devices. For the pristine device, a majority carrier mobility of 8×10^{-3} $cm^2\times V^{-1}\times s^{-1}$ has been used to fit the experimental data, in close agreement with the values obtained from IS analysis. In order to fit the S-shaped *J*-*V* curves for the degraded devices, the ATLAS model has been modified to include a degradation of the anode contact (decrease of its absolute work function) together with a partial degradation of the front active layer blend (~ 120 nm layer with reduced mobility near the anode contact) and an increased external series resistance. The parameter

values leading to best fits are shown in Table 4. They confirm that degradation is caused both by the active layer and the anode contact worsening.

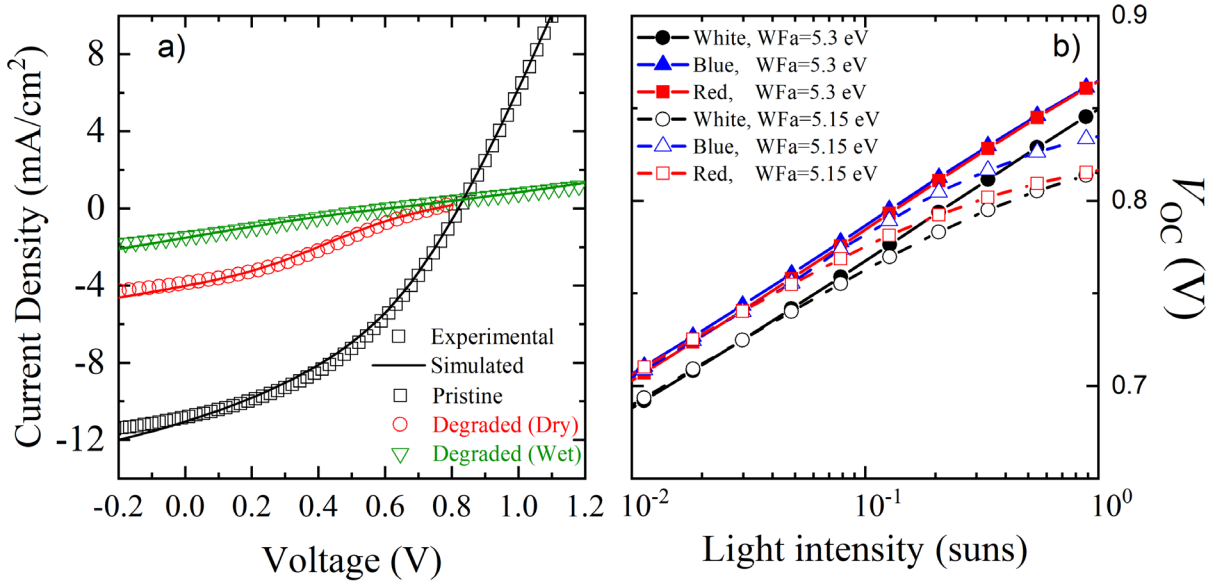

Figure 9. a) Experimental (symbols) and numerically simulated (lines) *J-V* characteristics under 1-sun illumination AM1.5 (100 mW/cm^2) for the pristine and degraded devices. b) V_{OC} vs light intensity obtained using white, blue and red illuminations, with an anode work function of 5.3 and 5.15 eV, reproducing the effect of the anode degradation.

Table 4. Parameters used in the simulations with Silvaco ATLAS for the pristine and degraded devices.

			Damaged active layer	
	Anode WF (eV)	Series resistance (Ω)	Mobility ($cm^2 \cdot V^{-1} \cdot s^{-1}$)	Depth (nm)
Pristine	5.30	42	8×10^{-3}	--
Degraded (dry)	5.15	80	5×10^{-4}	120
Degraded (wet)	5.00	300	4×10^{-4}	175

It should be emphasized that the good agreement between the experiment and the theory displayed in Figure 9a is achieved when both, the anode work function (WF) is reduced and the decreased mobility of a layer is introduced in the physical model. Several attempts to fit the experimental data only by changing the anode WF, or only by introducing a damaged layer did not lead to good fits.

As previously indicated, the ideality factor parameter can be obtained from the slope of the open-circuit potential (V_{OC}) vs. light intensity plot. Table 5 displays the n values extracted by simulating the evolution of V_{OC} with light intensity for two different anode WFs (see Figure 9b). These values agree with the trends of experimental n shown in Table 2. The ideality factors for red and white illumination decrease towards $n \approx 1$, while it remains almost unchanged for the blue light. In summary, numerical simulations confirm that these devices behave as p-i-n cell with accumulation of majority carriers at the contacts, and the degradation emphasizes SRH recombination near the anode (with $n \sim 1$) as the dominant recombination mechanism.

Table 5. Ideality factors for the fresh and the degraded cells extracted from the simulation results shown in Figure 9b using a theoretical model of the device under study for red, blue, and white light illumination.

	n		
	Red	Blue	White
Pristine	1.3	1.3	1.2
Degraded	1	1.2	0.9

These simulations agree well with experimental results and support the fact that degradation is caused by the combination of two mechanisms that are clearly observed when analyzing the

electrical behavior using two distinct wavelengths. On one hand, the change in the ideality factor shows a larger change for the red light when comparing fresh and degraded samples indicating that the degradation is affecting the space near the anode, where the red wavelength is being strongly absorbed. On the other hand, the mobility of the blend is also decreasing for the degraded devices, and this is observed in a more pronounced change in the absolute value of V_{OC} for the blue light (see fig. 3) that penetrates deeper in the bulk.

CONCLUSIONS

In summary, an analysis of ideality factors using red and blue incident light reveals a greater change of *n* for longer wavelengths when fresh and aged samples are compared, suggesting that recombination is specifically taking place in a region near the anode, where the red light is mainly being absorbed. Blue light penetrates deeper in the sample, and no significant change in *n* is obtained. Moreover, temperature measurements reveal SRH recombination through intermediate trap states with an activation energy smaller that the optical bandgap. IS parameters obtained from the fit to a standard equivalent circuit indicate an increase of the transport limiting mechanisms for the aged samples. This is also confirmed by the decrease in mobility of the degraded devices obtained for all illumination spectra. The increase of the chemical capacitance for the degraded samples indicates an accumulation of carriers due to a worsening of carrier extraction. In addition, the width of the density of states in the LUMO obtained from the chemical capacitance increases for the samples that underwent wet outdoor degradation, suggesting a higher degree of disorder of the blend under those conditions.

In addition, physical modelling and numerical simulations were carried out in order to support the conclusions obtained from the experiments. The simulations support the existence of an

interfacial damage layer near the anode contact with a worsened mobility. Moreover, good fits of the model to experimental *J-V* curves under illumination for the degraded samples were obtained only when the model takes into account both, a decreased mobility in a ~ 120 nm layer, and a reduced anode WF, confirming a worsening in charge extraction. Finally, simulations reveal a non-zero electric field across the active layer indicating that these cells behave as p-i-n devices with an accumulation of majority carriers near the contacts. Furthermore, ideality factors obtained from simulations are in good agreement with experimental values of $n \sim 1$ after degradation, reinforcing the enhanced dominant SRH recombination near the anode.

ASSOCIATED CONTENT

Supporting Information. The following files are available.

File "ArredondoEtAl_ae-2020-007118_SuppInfo", with statistical information of device performance, AFM images, degradation characterization details, device physical modelling and numerical simulations additional information (.docx)

AUTHOR INFORMATION

Corresponding Author

E-mail: belen.arredondo@urjc.es. Full-postal address: Universidad Rey Juan Carlos (Edificio Departamental II, despacho 158). C/ Tulipán s/n, 28933 Móstoles, Madrid.

Author Contributions

All authors contributed to the manuscript and were involved in the results discussion. J. L., E. D. V. T., M. M. manufactured the devices. D.M.M. performed the physical simulations. The rest of

the authors performed all the characterization and circuital modeling. B. A. wrote the manuscript with contributions from EHB, V.T and M.M. All authors have given approval to the final version of the manuscript.

Notes

The authors declare no competing financial interest.

Funding Sources

This work has been supported by Comunidad de Madrid under the SINFOTON2-CM Research Program (S2018/NMT-4326-SINFOTON2-CM) and the Spanish Ministry of Economy, the Agencia Estatal de Investigación and European Union's FEDER under the TEC2016-77242-C1/C2/C3 AEI/FEDER, UE Projects. The work of E. López- Fraguas was supported by the Ministerio de Educación y Formación Profesional for his Doctoral Grant through FPU Research Fellowship under Grant FPU17/00612. M.M., J.L, E.D. and V.T. acknowledge that part of this work has been developed within the RollFlex project, part-financed by Interreg Deutschland-Danmark with means from the European Regional Development Fund and the Southern Denmark Growth Forum. M.M. and V.T. acknowledge the support from the Villum Foundation for Project CompliantPV (Grant No. 13365). Finally, all authors acknowledge the support from EU Framework Programme Horizon 2020 for MNPS COST ACTION MP1307 StableNextSol.

ABBREVIATIONS

BHJ, bulk heterojunction; CPE, Constant Phase Element; DOS, Density of States; EQE, External Quantum Efficiency; FF, Fill Factor; HUMO, Highest Unoccupied Molecular Orbital; IDL, Internal Damaged Layer; IS, Impedance Spectroscopy; LUMO, Lowest Unoccupied Molecular Orbital; NFA, Non-Fullerene Acceptor; OPV, Organic PhotoVoltaic; OSC, Organic Solar Cell;

PCE, Power Conversion Efficiency; R2R, Roll to Roll; SRH, Shockley-Read-Hall; WF, Work Function.

REFERENCES

(1) Ganesamoorthy, R.; Sathiyan, G.; Sakthivel, P. Review: Fullerene Based Acceptors for Efficient Bulk Heterojunction Organic Solar Cell Applications. *Solar Energy Materials and Solar Cells* **2017**, *161*, 102–148. https://doi.org/10.1016/j.solmat.2016.11.024.

(2) Chen, J.-D.; Cui, C.; Li, Y.-Q.; Zhou, L.; Ou, Q.-D.; Li, C.; Li, Y.; Tang, J.-X. Single-Junction Polymer Solar Cells Exceeding 10% Power Conversion Efficiency. *Advanced Materials* **2015**, *27* (6), 1035–1041. https://doi.org/10.1002/adma.201404535.

(3) Liu, C.; Yi, C.; Wang, K.; Yang, Y.; Bhatta, R. S.; Tsige, M.; Xiao, S.; Gong, X. Single-Junction Polymer Solar Cells with over 10% Efficiency by a Novel Two-Dimensional Donor-Acceptor Conjugated Copolymer. *ACS Appl Mater Interfaces* **2015**, *7* (8), 4928–4935. https://doi.org/10.1021/am509047g.

(4) Liao, S.-H.; Jhuo, H.-J.; Yeh, P.-N.; Cheng, Y.-S.; Li, Y.-L.; Lee, Y.-H.; Sharma, S.; Chen, S.-A. Single Junction Inverted Polymer Solar Cell Reaching Power Conversion Efficiency 10.31% by Employing Dual-Doped Zinc Oxide Nano-Film as Cathode Interlayer. *Scientific Reports* **2014**, *4*, 6813. https://doi.org/10.1038/srep06813.

(5) Arredondo, B.; Romero, B.; Beliatis, M. J.; del Pozo, G.; Martín-Martín, D.; Blakesley, J. C.; Dibb, G.; Krebs, F. C.; Gevorgyan, S. A.; Castro, F. A. Analysing Impact of Oxygen and Water Exposure on Roll-Coated Organic Solar Cell Performance Using Impedance Spectroscopy. *Solar Energy Materials and Solar Cells* **2018**, *176*, 397–404. https://doi.org/10.1016/j.solmat.2017.10.028.

(6) Gupta, S. K.; Pali, L. S.; Garg, A. Impedance Spectroscopy on Degradation Analysis of Polymer/Fullerene Solar Cells. *Solar Energy* **2019**, *178*, 133–141. https://doi.org/10.1016/j.solener.2018.12.024.

(7) Sherafatipour, G.; Benduhn, J.; Patil, B. R.; Ahmadpour, M.; Spoltore, D.; Rubahn, H.-G.; Vandewal, K.; Madsen, M. Degradation Pathways in Standard and Inverted DBP-C 70 Based Organic Solar Cells. *Scientific Reports* **2019**, *9* (1), 4024. https://doi.org/10.1038/s41598-019-40541-6.

(8) Wang, Y.; Jafari, M. J.; Wang, N.; Qian, D.; Zhang, F.; Ederth, T.; Moons, E.; Wang, J.; Inganäs, O.; Huang, W.; Gao, F. Light-Induced Degradation of Fullerenes in Organic Solar Cells: A Case Study on TQ1:PC71BM. *J. Mater. Chem. A* **2018**, *6* (25), 11884–11889. https://doi.org/10.1039/C8TA03112F.

(9) Andreasen, B.; Tanenbaum, D. M.; Hermenau, M.; Voroshazi, E.; Lloyd, M. T.; Galagan, Y.; Zimmernann, B.; Kudret, S.; Maes, W.; Lutsen, L.; Vanderzande, D.; Würfel, U.; Andriessen, R.; Rösch, R.; Hoppe, H.; Teran-Escobar, G.; Lira-Cantu, M.; Rivaton, A.; Uzunoğlu, G. Y.; Germack, D. S.; Hösel, M.; Dam, H. F.; Jørgensen, M.; Gevorgyan, S. A.; Madsen, M. V.; Bundgaard, E.; Krebs, F. C.; Norrman, K. TOF-SIMS Investigation of Degradation Pathways Occurring in a Variety of Organic Photovoltaic Devices--the ISOS-3 Inter-Laboratory Collaboration. *Phys Chem Chem Phys* **2012**, *14* (33), 11780–11799. https://doi.org/10.1039/c2cp41787a.

(10) Rösch, R.; Tanenbaum, D. M.; Jørgensen, M.; Seeland, M.; Bärenklau, M.; Hermenau, M.; Voroshazi, E.; Lloyd, M. T.; Galagan, Y.; Zimmermann, B.; Würfel, U.; Hösel, M.; Dam, H. F.; Gevorgyan, S. A.; Kudret, S.; Maes, W.; Lutsen, L.; Vanderzande, D.; Andriessen, R.; Teran-Escobar, G.; Lira-Cantu, M.; Rivaton, A.; Uzunoğlu, G. Y.; Germack, D.; Andreasen, B.; Madsen, M. V.; Norrman, K.; Hoppe, H.; Krebs, F. C. Investigation of the Degradation Mechanisms of a Variety of Organic Photovoltaic Devices by Combination of Imaging Techniques—the ISOS-3 Inter-Laboratory Collaboration. *Energy Environ. Sci.* **2012**, *5* (4), 6521–6540. https://doi.org/10.1039/C2EE03508A.

(11) Tanenbaum, D. M.; Hermenau, M.; Voroshazi, E.; Lloyd, M. T.; Galagan, Y.; Zimmermann, B.; Hösel, M.; Dam, H. F.; Jørgensen, M.; Gevorgyan, S. A.; Kudret, S.; Maes, W.; Lutsen, L.; Vanderzande, D.; Würfel, U.; Andriessen, R.; Rösch, R.; Hoppe, H.; Teran-Escobar, G.; Lira-Cantu, M.; Rivaton, A.; Uzunoğlu, G. Y.; Germack, D.; Andreasen, B.; Madsen, M. V.; Norrman, K.; Krebs, F. C. The ISOS-3 Inter-Laboratory Collaboration Focused on the Stability of a Variety of Organic Photovoltaic Devices. *RSC Adv.* **2012**, *2* (3), 882–893. https://doi.org/10.1039/C1RA00686J.

(12) Turkovic, V.; Engmann, S.; Tsierkezos, N.; Hoppe, H.; Madsen, M.; Rubahn, H.-G.; Ritter, U.; Gobsch, G. Long-Term Stabilization of Organic Solar Cells Using Hydroperoxide Decomposers as Additives. *Appl. Phys. A* **2016**, *122* (3), 255. https://doi.org/10.1007/s00339-016-9758-7.

(13) Turkovic, V.; Prete, M.; Bregnhøj, M.; Inasaridze, L.; Volyniuk, D.; Obrezkov, F. A.; Grazulevicius, J. V.; Engmann, S.; Rubahn, H.-G.; Troshin, P. A.; Ogilby, P. R.; Madsen, M. Biomimetic Approach to Inhibition of Photooxidation in Organic Solar Cells Using Beta-Carotene as an Additive. *ACS Appl. Mater. Interfaces* **2019**, *11* (44), 41570–41579. https://doi.org/10.1021/acsami.9b13085.

(14) Zhao, W.; Qian, D.; Zhang, S.; Li, S.; Inganäs, O.; Gao, F.; Hou, J. Fullerene-Free Polymer Solar Cells with over 11% Efficiency and Excellent Thermal Stability. *Advanced Materials* **2016**, *28* (23), 4734–4739. https://doi.org/10.1002/adma.201600281.

(15) Upama, M. B.; Wright, M.; Mahmud, M. A.; Elumalai, N. K.; Soufiani, A. M.; Wang, D.; Xu, C.; Uddin, A. Photo-Degradation of High Efficiency Fullerene-Free Polymer Solar Cells. *Nanoscale* **2017**, *9* (47), 18788–18797. https://doi.org/10.1039/C7NR06151J.

(16) An, Q.; Zhang, F.; Gao, W.; Sun, Q.; Zhang, M.; Yang, C.; Zhang, J. High-Efficiency and Air Stable Fullerene-Free Ternary Organic Solar Cells. *Nano Energy* **2018**, *45*, 177–183. https://doi.org/10.1016/j.nanoen.2017.12.050.

(17) Li, S.; Ye, L.; Zhao, W.; Zhang, S.; Mukherjee, S.; Ade, H.; Hou, J. Energy-Level Modulation of Small-Molecule Electron Acceptors to Achieve over 12% Efficiency in Polymer Solar Cells. *Advanced Materials* **2016**, *28* (42), 9423–9429. https://doi.org/10.1002/adma.201602776.

(18) Li, S.; Ye, L.; Zhao, W.; Yan, H.; Yang, B.; Liu, D.; Li, W.; Ade, H.; Hou, J. A Wide Band Gap Polymer with a Deep Highest Occupied Molecular Orbital Level Enables 14.2% Efficiency in Polymer Solar Cells. *J. Am. Chem. Soc.* **2018**, *140* (23), 7159–7167. https://doi.org/10.1021/jacs.8b02695.

(19) Speller, E. M.; Clarke, A. J.; Aristidou, N.; Wyatt, M. F.; Francàs, L.; Fish, G.; Cha, H.; Lee, H. K. H.; Luke, J.; Wadsworth, A.; Evans, A. D.; McCulloch, I.; Kim, J.-S.; Haque, S. A.; Durrant, J. R.; Dimitrov, S. D.; Tsoi, W. C.; Li, Z. Toward Improved Environmental Stability of Polymer:Fullerene and Polymer:Nonfullerene Organic Solar Cells: A

Common Energetic Origin of Light- and Oxygen-Induced Degradation. *ACS Energy Lett.* **2019**, *4* (4), 846–852. https://doi.org/10.1021/acsenergylett.9b00109.
(20) Yan, C.; Barlow, S.; Wang, Z.; Yan, H.; Jen, A. K.-Y.; Marder, S. R.; Zhan, X. Non-Fullerene Acceptors for Organic Solar Cells. *Nature Reviews Materials* **2018**, *3* (3), 18003. https://doi.org/10.1038/natrevmats.2018.3.
(21) Cui, Y.; Yao, H.; Zhang, J.; Zhang, T.; Wang, Y.; Hong, L.; Xian, K.; Xu, B.; Zhang, S.; Peng, J.; Wei, Z.; Gao, F.; Hou, J. Over 16% Efficiency Organic Photovoltaic Cells Enabled by a Chlorinated Acceptor with Increased Open-Circuit Voltages. *Nature Communications* **2019**, *10* (1), 2515. https://doi.org/10.1038/s41467-019-10351-5.
(22) Fan, B.; Zhang, D.; Li, M.; Zhong, W.; Zeng, Z.; Ying, L.; Huang, F.; Cao, Y. Achieving over 16% Efficiency for Single-Junction Organic Solar Cells. *Sci. China Chem.* **2019**, *62* (6), 746–752. https://doi.org/10.1007/s11426-019-9457-5.
(23) Zhang, S.; Qin, Y.; Zhu, J.; Hou, J. Over 14% Efficiency in Polymer Solar Cells Enabled by a Chlorinated Polymer Donor. *Advanced Materials* **2018**, *30* (20), 1800868. https://doi.org/10.1002/adma.201800868.
(24) Zheng, Z.; Hu, Q.; Zhang, S.; Zhang, D.; Wang, J.; Xie, S.; Wang, R.; Qin, Y.; Li, W.; Hong, L.; Liang, N.; Liu, F.; Zhang, Y.; Wei, Z.; Tang, Z.; Russell, T. P.; Hou, J.; Zhou, H. A Highly Efficient Non-Fullerene Organic Solar Cell with a Fill Factor over 0.80 Enabled by a Fine-Tuned Hole-Transporting Layer. *Advanced Materials* **2018**, *30* (34), 1801801. https://doi.org/10.1002/adma.201801801.
(25) Baran, D.; Kirchartz, T.; Wheeler, S.; Dimitrov, S.; Abdelsamie, M.; Gorman, J.; Ashraf, R. S.; Holliday, S.; Wadsworth, A.; Gasparini, N.; Kaienburg, P.; Yan, H.; Amassian, A.; Brabec, C. J.; Durrant, J. R.; McCulloch, I. Reduced Voltage Losses Yield 10% Efficient Fullerene Free Organic Solar Cells with >1 V Open Circuit Voltages. *Energy Environ. Sci.* **2016**, *9* (12), 3783–3793. https://doi.org/10.1039/C6EE02598F.
(26) Qian, D.; Zheng, Z.; Yao, H.; Tress, W.; Hopper, T. R.; Chen, S.; Li, S.; Liu, J.; Chen, S.; Zhang, J.; Liu, X.-K.; Gao, B.; Ouyang, L.; Jin, Y.; Pozina, G.; Buyanova, I. A.; Chen, W. M.; Inganäs, O.; Coropceanu, V.; Bredas, J.-L.; Yan, H.; Hou, J.; Zhang, F.; Bakulin, A. A.; Gao, F. Design Rules for Minimizing Voltage Losses in High-Efficiency Organic Solar Cells. *Nature Materials* **2018**, *17* (8), 703. https://doi.org/10.1038/s41563-018-0128-z.
(27) Holliday, S.; Ashraf, R. S.; Wadsworth, A.; Baran, D.; Yousaf, S. A.; Nielsen, C. B.; Tan, C.-H.; Dimitrov, S. D.; Shang, Z.; Gasparini, N.; Alamoudi, M.; Laquai, F.; Brabec, C. J.; Salleo, A.; Durrant, J. R.; McCulloch, I. High-Efficiency and Air-Stable P3HT-Based Polymer Solar Cells with a New Non-Fullerene Acceptor. *Nat Commun* **2016**, *7*, 11585. https://doi.org/10.1038/ncomms11585.
(28) Lin, Y.; Zhao, F.; He, Q.; Huo, L.; Wu, Y.; Parker, T. C.; Ma, W.; Sun, Y.; Wang, C.; Zhu, D.; Heeger, A. J.; Marder, S. R.; Zhan, X. High-Performance Electron Acceptor with Thienyl Side Chains for Organic Photovoltaics. *J. Am. Chem. Soc.* **2016**, *138* (14), 4955–4961. https://doi.org/10.1021/jacs.6b02004.
(29) Doumon, N. Y.; Dryzhov, M. V.; Houard, F. V.; Le Corre, V. M.; Rahimi Chatri, A.; Christodoulis, P.; Koster, L. J. A. Photostability of Fullerene and Non-Fullerene Polymer Solar Cells: The Role of the Acceptor. *ACS Appl. Mater. Interfaces* **2019**, *11* (8), 8310–8318. https://doi.org/10.1021/acsami.8b20493.
(30) Du, X.; Heumueller, T.; Gruber, W.; Classen, A.; Unruh, T.; Li, N.; Brabec, C. J. Efficient Polymer Solar Cells Based on Non-Fullerene Acceptors with Potential Device Lifetime

Approaching 10 Years. *Joule* **2019**, *3* (1), 215–226. https://doi.org/10.1016/j.joule.2018.09.001.
(31) Luke, J.; Speller, E. M.; Wadsworth, A.; Wyatt, M. F.; Dimitrov, S.; Lee, H. K. H.; Li, Z.; Tsoi, W. C.; McCulloch, I.; Bagnis, D.; Durrant, J. R.; Kim, J.-S. Twist and Degrade—Impact of Molecular Structure on the Photostability of Nonfullerene Acceptors and Their Photovoltaic Blends. *Advanced Energy Materials* **2019**, *9* (15), 1803755. https://doi.org/10.1002/aenm.201803755.
(32) Destouesse, E.; Top, M.; Lamminaho, J.; Rubahn, H.-G.; Fahlteich, J.; Madsen, M. Slot-Die Processing and Encapsulation of Non-Fullerene Based ITO-Free Organic Solar Cells and Modules. *Flex. Print. Electron.* **2019**, *4* (4), 045004. https://doi.org/10.1088/2058-8585/ab556f.
(33) Reese, M. O.; Gevorgyan, S. A.; Jørgensen, M.; Bundgaard, E.; Kurtz, S. R.; Ginley, D. S.; Olson, D. C.; Lloyd, M. T.; Morvillo, P.; Katz, E. A.; Elschner, A.; Haillant, O.; Currier, T. R.; Shrotriya, V.; Hermenau, M.; Riede, M.; R. Kirov, K.; Trimmel, G.; Rath, T.; Inganäs, O.; Zhang, F.; Andersson, M.; Tvingstedt, K.; Lira-Cantu, M.; Laird, D.; McGuiness, C.; Gowrisanker, S. (Jimmy); Pannone, M.; Xiao, M.; Hauch, J.; Steim, R.; DeLongchamp, D. M.; Rösch, R.; Hoppe, H.; Espinosa, N.; Urbina, A.; Yaman-Uzunoglu, G.; Bonekamp, J.-B.; van Breemen, A. J. J. M.; Girotto, C.; Voroshazi, E.; Krebs, F. C. Consensus Stability Testing Protocols for Organic Photovoltaic Materials and Devices. *Solar Energy Materials and Solar Cells* **2011**, *95* (5), 1253–1267. https://doi.org/10.1016/j.solmat.2011.01.036.
(34) López-Fraguas, E.; Sánchez-Pena, J. M.; Vergaz, R. A Low-Cost LED-Based Solar Simulator. *IEEE Transactions on Instrumentation and Measurement* **2019**, 1–11. https://doi.org/10.1109/TIM.2019.2899513.
(35) Yao, H.; Cui, Y.; Yu, R.; Gao, B.; Zhang, H.; Hou, J. Design, Synthesis, and Photovoltaic Characterization of a Small Molecular Acceptor with an Ultra-Narrow Band Gap. *Angewandte Chemie International Edition* **2017**, *56* (11), 3045–3049. https://doi.org/10.1002/anie.201610944.
(36) Wang, T.-L.; Yang, C.-H.; Chuang, Y.-Y. A Comparative Study of the Effect of Fluorine Substitution on the Photovoltaic Performance of Benzothiadiazole-Based Copolymers. *RSC Adv.* **2016**, *6* (53), 47676–47686. https://doi.org/10.1039/C6RA05062J.
(37) Jørgensen, M.; Norrman, K.; Gevorgyan, S. A.; Tromholt, T.; Andreasen, B.; Krebs, F. C. Stability of Polymer Solar Cells. *Advanced Materials* **2012**, *24* (5), 580–612. https://doi.org/10.1002/adma.201104187.
(38) Xu, T.; Gong, C.; Wang, S.; Lian, H.; Lan, W.; Lévêque, G.; Grandidier, B.; Plain, J.; Bachelot, R.; Wei, B.; Zhu, F. Ultraviolet-Durable Flexible Nonfullerene Organic Solar Cells Realized by a Hybrid Nanostructured Transparent Electrode. *Solar RRL* **2020**, *4* (5), 1900522. https://doi.org/10.1002/solr.201900522.
(39) Tress, W.; Yavari, M.; Domanski, K.; Yadav, P.; Niesen, B.; Baena, J. P. C.; Hagfeldt, A.; Graetzel, M. Interpretation and Evolution of Open-Circuit Voltage, Recombination, Ideality Factor and Subgap Defect States during Reversible Light-Soaking and Irreversible Degradation of Perovskite Solar Cells. *Energy Environ. Sci.* **2018**, *11* (1), 151–165. https://doi.org/10.1039/C7EE02415K.
(40) Wang, Y.; Lan, W.; Li, N.; Lan, Z.; Li, Z.; Jia, J.; Zhu, F. Stability of Nonfullerene Organic Solar Cells: From Built-in Potential and Interfacial Passivation Perspectives.

Advanced Energy Materials **2019**, *9* (19), 1900157. https://doi.org/10.1002/aenm.201900157.
(41) Qi, B.; Wang, J. Fill Factor in Organic Solar Cells. *Phys. Chem. Chem. Phys.* **2013**, *15* (23), 8972–8982. https://doi.org/10.1039/C3CP51383A.
(42) Hirschorn, B.; Orazem, M. E.; Tribollet, B.; Vivier, V.; Frateur, I.; Musiani, M. Determination of Effective Capacitance and Film Thickness from Constant-Phase-Element Parameters. *Electrochimica Acta* **2010**, *55* (21), 6218–6227. https://doi.org/10.1016/j.electacta.2009.10.065.
(43) Bässler, H. Charge Transport in Disordered Organic Photoconductors a Monte Carlo Simulation Study. *physica status solidi (b)* **1993**, *175* (1), 15–56. https://doi.org/10.1002/pssb.2221750102.
(44) Interdependence of absorber composition and recombination mechanism in Cu(In,Ga)(Se,S)2 heterojunction solar cells: Applied Physics Letters: Vol 80, No 14 https://aip.scitation.org/doi/10.1063/1.1467621 (accessed Sep 23, 2019).

TOC Graphic. For Table of Contents use only.